

Prospective earthquake forecasts at the Himalayan front after the 25 April 2015 $M=7.8$ Gorkha mainshock

Accepted for publication

Seismological Research Letters

Margarita Segou¹ and Tom Parsons²

1. British Geological Survey, Edinburgh, UK 2. U.S. Geological Survey, Menlo Park, California

When a major earthquake strikes, the resulting devastation can be compounded or even exceeded by the subsequent cascade of triggered seismicity. As the Nepalese recover from the 25 April 2015 shock, knowledge of what comes next is essential. We calculate the redistribution of crustal stresses and implied earthquake probabilities for different periods from daily to 30 years into the future. An initial forecast was completed before a $M=7.3$ earthquake struck on May 12, 2015 that enables a preliminary assessment; post-forecast seismicity has so far occurred within a zone of 5-fold probability gain. Evaluation of the forecast performance, using 2 months of seismic data, reveals that stress-based approaches present improved skill in higher magnitude triggered seismicity. Our results suggest that considering the total stress field, rather than only the co-seismic one, improves the spatial performance of the model based on the estimation of a wide range of potential triggered faults following a mainshock.

Introduction

The Himalayas rise by absorbing 18-22 mm/yr of Indian-Eurasian plate convergence (Ader *et al.*, 2012) (Fig. 1). On the 25th of April, 2015, a $M=7.8$ earthquake ruptured the low-angle (10°) fault contact between the two plates, leading to more than 8000 confirmed fatalities, 18,000 people injured, and a million families affected (Nepal Red Cross Society¹). Eight UNESCO World Heritage sites were damaged or destroyed. The 25 April shock struck the eastern edge of a 500-km-wide gap between historic earthquakes along the Himalayan front (Fig. 1). The potential of triggered earthquakes beneath highly populated basins in the central Himalaya could compound this catastrophe akin to tragedies in Turkey (Parsons *et al.*, 2000), China (Parsons *et al.*, 2008), and New Zealand (Stramondo *et al.*, 2011). Recent studies, based on retrospective experiments, investigate the predictive power of short-term earthquake forecasts within different distance ranges and periods (Segou *et al.*, 2013; Strader and Jackson, 2015), but prospective forecasts still face challenges such as the quality of real-time data, the availability of credible historical/modern earthquake catalogs, and very short research windows.

In this study, we calculate the expected redistribution of stress in the Himalayan crust and develop a method, especially applicable to frontier regions, to determine the probability of triggered earthquakes in both space and time. We make prospective earthquake forecasts using four methods incorporating physics-based and statistical approaches for varying time horizons, and formally evaluate the shortest-term calculations.

The results reveal the efficiency of physics-based forecasts in estimating short-term earthquake probabilities and their critical contribution in modeling off-fault triggered events, highlighted by the $M=5.6$ Xegar (3 hours after the mainshock) and the $M=7.3$ Kodari (May 12) earthquakes.

Development of Short-Term Earthquake Forecasts

Short-term earthquake forecasts can use empirical statistics to anticipate cascades of triggered events, or simulations of stress redistribution following a mainshock combined with conceptual friction models to describe triggered earthquake occurrence (Harris, 1998; Stein, 1999). Neither method flawlessly accounts for the spectrum of post mainshock earthquake behavior (e.g., Nanjo *et al.*, 2012; Cocco *et al.*, 2010; Segou *et al.*, 2014). Empirical/statistical models depend heavily on the density of the local seismic network and identification of precursory activity and are thus vulnerable in frontier regions. In this study, we employ an Epidemic Type Aftershock Sequence (ETAS) model as a benchmark to compare the efficiency of our physics-based forecasts in capturing all possible triggering mechanisms (Ogata, 1988; Ogata, 1998; see ETAS implementation section, available in the electronic supplement to this article).

¹ Available information at <http://www.nrcs.org>

Physics-based models depend on accurate simulation of a mainshock rupture and its transfer of stress onto neighboring active crustal faults. In this context Coulomb failure stress is described by the equation

$$\Delta CF = \Delta |\bar{\tau}_f| + \mu' (\Delta \sigma_n) \quad (1)$$

where $\Delta |\bar{\tau}_f|$ is the change in shear stress on the receiver fault, $\Delta \sigma_n$ is the change in normal stress, $\mu' = \mu(1 - B_k)$ is the effective coefficient of friction, and B_k is Skempton's coefficient that accounts for pore fluid pressure effects. Stress values are found by slipping an elastic dislocation representation of the mainshock slip model provided by USGS in near-real time, and calculating Coulomb failure stress changes on hypothetical faults optimally oriented to the regional stress field (King et al., 1994; Harris, 1998), wherein faults may be brought closer to, or further from failure. The friction coefficient is taken to be $\mu=0.4$ in all cases for uniform comparison. A 10 MPa deviatoric tectonic stress with compression oriented N19°E (Jouanne et al., 2004; Bollinger et al., 2004) is used to find optimally oriented receiver fault planes. Additionally, we calculate stress change on planes parallel to, and on the mainshock fault to find likely future rupture areas on the main boundary fault and other possibly hidden faults of like orientation (Wobus et al., 2005). All maps of stress change in the manuscript are shown at 10 km depth, which is where the majority of aftershocks were located during the first 5 days after the mainshock.

In order to convert calculated stress changes to forecast earthquake rates, we follow the rate-and-state friction framework (Dieterich, 1994; Dieterich, 1996) where the pre-mainshock earthquake activity r and the time-dependent seismicity rate R we aim to predict are connected through the

$$\text{equation, } R = \frac{r}{\gamma \dot{\tau}}, \quad (2)$$

$$\text{where } \gamma_n = \gamma_{n-1} \exp\left(\frac{-\Delta CF}{\alpha \sigma}\right) \quad (3)$$

The decay rate of the stress effect ΔCF is inversely correlated with the shear-stressing rate ($\dot{\tau}$) as taken from the relation $t_\alpha = \frac{\alpha \sigma}{\dot{\tau}}$, where t_α is the aftershock duration, and $\alpha \sigma$ is a fault constitutive parameter (see *Conversion of stress changes to forecast earthquake rates* section, available in the electronic supplement to this article).

A persistent problem with physical models is that triggered earthquakes often happen in areas of calculated stress reduction known as stress shadows (Harris and Simpson, 1996), where theoretically they should be suppressed (Mallman and Zoback, 2007; Parsons et al., 2012). We thus develop an approach to address the issue of calculated stress decreases that we call the total stress method. The total stress calculation reports the complete (preseismic and coseismic) stress field rather than just coseismic changes because aftershocks may be responding to the regional stress field on non-optimal planes in areas where there are calculated coseismic stress decreases. In this mode there are no expected regions of earthquake suppression because there is always a possible fault orientation that is favorable for failure. Therefore certain earthquake mechanisms may be suppressed, but others are encouraged (Mallman and Parsons, 2008; Hardebeck, 2014).

The total stress method differs from standard stress change methods, but shares the following traits: the total stress tensor is the sum of the pre-mainshock stress (based on N19°E-directed 10-MPa-deviatoric stress) and stress-change tensors

$$\sigma_{x,y,z}^T = \sigma_{x,y,z}^{PRE} + \Delta\sigma_{x,y,z} \quad (4)$$

The post-mainshock principal stress axes are the diagonal components of the tensor rotated such that the shear components are zero. Following Jaeger and Cook (1976), the strike angle between principal stress axes and the theoretical maximum stress-change fault plane β is from $\tan(2\beta) = 1/\mu$. At this point, methods in general use (King *et al.*, 1994; Toda *et al.*, 2005; Toda and Enescu, 2011) calculate stress changes that are determined only by the earthquake stress changes on these planes, which can be positive or negative. The total stress method differs because in an earthquake prone region with strong differential stress, it is almost always possible to find a fault orientation where Coulomb failure is favored. An example highlighting the importance of the total stress methods for Northern California is available to the electronic supplement of this paper. (Fig. S1). To find these failure planes, a grid search is performed in 5° steps over dip and rake to maximize Coulomb failure for all possible mechanism classes (reverse, normal, and transform).

As destructive as the 2015 Gorkha earthquake was, interpretation of paleoseismological (Rajendran *et al.*, 2015; Bollinger *et al.*, 2014; Sakopta *et al.*, 2013) and historical shaking intensity observations shows that earthquakes well above $M=8$ occur routinely along the Himalayan front (Bilham *et al.*, 2001) (Fig. 1). Therefore, in order to gain some sense of the impact of the 25 April $M=7.8$ mainshock on future earthquakes along the Main Himalayan thrust, we also make time-dependent probability calculations (e.g. Parsons *et al.*, 2010; Console *et al.*, 2010). We estimate time dependent probability using a Brownian Passage Time (BPT) distribution with aperiodicity=0.5 and bracket the calculations with mean recurrence intervals ranging from 750-870 years and last earthquake times either 1255 or 1505 (Rajendran *et al.*, 2015; Bollinger *et al.*, 2014; Sakopta *et al.*, 2013). Hardebeck (2004) discusses about the importance of the assumptions in using BPT distribution together within rate-and-state framework, while Parsons (2005) notes the significance behind using stress changes in estimating time-dependent probabilities when the latter are considerably greater than the calculated tectonic stressing rate.

RESULTS

We find that traditional stress change calculations resolved on faults parallel to the mainshock and onto optimal faults cannot fully explain the first 5 days of triggered earthquakes after the 25 April mainshock. The total stress method greatly increases the array of possible failure planes, and more closely represents complex tectonic environments like Nepal, which has thrust, strike-slip, and normal faults in close proximity (Yeats *et al.*, 1992). This exercise does not produce stress shadows since the total stress is always positive. We find only 12% of events (Fig. 2c) triggered by the 25 April 2015 Nepal mainshock happening in areas where the maximum total stress is less than the pre-seismic levels, which would be conceptually similar to a stress shadow. By contrast, standard methods have 48%-72% of triggered events (Fig. 2a-b) happening in areas with calculated stress reduction. We note that all methods show the Katmandu basin under a co-seismic stress increase.

We estimate an average stress increase of 0.15 MPa for the Thankot fault ($M_{max}\sim 6.6$), located at the southwest edge of the Katmandu basin. To the southwest, calculations show stress increased by 0.32 MPa on the Kulekhani fault ($M_{max}\sim 6.9$) (NSET report, 2010). Stress was increased by 0.28 MPa on the Kalphu-Khola fault ($M_{max}\sim 6.9$) north of Katmandu. Nepal's

second largest city, Pokhara, lies to the west of the 25 April rupture and had a smaller coseismic stress increase (0.05 MPa) than in the Katmandu basin. Aggregated probability from mapped faults in the Katmandu Basin shows a 90% chance of at least one more $M \geq 4.7$ shock in the next 5 years.

We calculate up to 0.1 MPa coseismic stress increase on the deep decollement beneath the Himalayas (Fig 2d), and a 0.65 MPa increase on the main boundary thrust immediately west of the 2015 mainshock rupture.

We estimate the spatio-temporal distribution of triggered earthquakes above the magnitude completeness level of $M \geq 4.7$ within daily time intervals. The total-stress forecast predicted higher (relative to other methods) earthquake rates along an extended part the Himalayan front, including triggered seismicity in rift basins that cut across the Himalayas (Fig. 3d). We find evidence for widespread triggered seismicity during the initial hours, as demonstrated by the $M=5.7$ Xegar event 245 km east of the mainshock.

Our benchmark ETAS model shows signs of under-forecasting (Fig. 3a) because epidemic-type forecasts (earthquake cascades) rely on smaller magnitude events that tend to be unreported in Nepal. Statistical models perform best when local earthquake networks are capable of providing the highest quality data (Helmstetter, 2003). The two initial 5-day forecasts we produced based on standard physics (Fig. 3b-c) also underforecast the early triggered earthquake rates and were spatially limited, failing to capture the breadth of the triggered earthquake region.

A $M=7.3$ earthquake struck Nepal at Kodari on 12 May 2015, 17 days after, and 157 km away from the 25 April 2015 $M=7.8$ mainshock. This second large earthquake inflicted further casualties and damage to a region already impacted by the initial shock, and exemplifies the purpose of making post-mainshock earthquake forecasts. Our prospective earthquake forecast was submitted to the American Association for the Advancement of Science (AAAS) on 9 May 2015 (available in the electronic supplement to this article), 56 hours before the $M=7.3$ event occurred; this timing enables us to assess forecast performance prospectively.

The $M=7.3$ Kodari event struck within a zone where we calculated elevated probability, with 27% odds of a $M \geq 4.7$ in 5 years (9-fold probability gain over the pre-mainshock value of ~3%) (Fig. 4). All regional $M \geq 4.7$ seismicity between 25 April and 10 August 2015 has occurred within a zone of 5-fold probability gain over background. We calculated a 0.05 MPa stress increase at the future hypocenter of the $M=7.3$ shock, and that the most likely rupture would strike 327° , dip 34° , and have a 135° rake. Observed rupture parameters² are: strike= 303° , dip= 9° , and rake= 110° . Uncertainties in determining these values from seismograms are typically $\pm 20^\circ$ (Kagan, 2003). We therefore conclude that the 12 May 2015 $M=7.3$ event was triggered by the $M=7.8$ mainshock.

Following the standards set by the International Commission on Earthquake Forecasting in the aftermath of the catastrophic 2009 L'Aquila earthquake in Italy, an earthquake forecast has to

² Rupture mechanism for the greater triggered event is available at:

http://earthquake.usgs.gov/earthquakes/eventpage/us20002ejl#scientific_tensor

exhibit reliability and skill. The forecast models are updated to incorporate the stress effects of the $M=7.3$ Kodari triggered event, and the available earthquake information for 2 months following the mainshock. We employ a performance evaluation using statistical metrics suggested through the framework of the Collaboratory of the Study of Earthquake Predictability (CSEP) in recent literature (Jordan *et al.*, 2011; Rhoades *et al.*, 2011; Schorlemmer *et al.*, 2007; Zechar *et al.*, 2010; Woessner *et al.*, 2011).

The tested models are updated to incorporate the stress effects of the $M=7.3$ triggered event. Furthermore, we provide a map-view comparison between the initial and updated forecasts based on the total-stress method plotted with the observed seismicity (Fig. 5). The $M=7.3$ event raises the expected number in almost all active parts of the study grid, yet most activity so far is concentrated near the $M>7$ shocks.

We implement the modified N -, S -, and T -tests to evaluate the absolute (Fig. 6) and relative (Fig. 7) performance of the updated forecast models within 10 day windows after the $M=7.8$ Nepal mainshock. Within these windows, 36, 21, 3, 1, 2, and 1 $M\geq 4.7$ earthquake(s) occurred, characterizing a low-productivity sequence. The tests focus on the first 20 days (0-10, 10-20 days time intervals) following the mainshock because there are not enough events over the period from 20-60 days to make meaningful calculations. We note that the benchmark ETAS model uses all available triggered events within the aforementioned time intervals.

The results suggest that: (1) the statistical, standard physics-based, and total stress forecast models are do not pass the test due to underestimation and overestimation of the observed seismicity, reflected by the corresponding small δ_1 and δ_2 values, respectively. (2) The mean log-likelihood per spatial bin in triggered earthquake locations for the period immediately following the mainshock reveals that the total stress method achieves better spatial performance ($LL_s^{\text{Total}}=-1.12$), followed by physics-based optimal, parallel faults, and then the statistical model ($LL_s^{\text{Optimal}}=-3.22$, $LL_s^{\text{Parallel}}=-5.96$, $LL_s^{\text{ETAS}}=-8.78$). (3) Physics-based models outperform the standard physics-based and statistical models in locations of $M>6$ triggered events following the mainshock as expressed by the sum of log-likelihood during each time period (0-10, 10-20 days). In that context we note that $jLL_s^{\text{Total}}=-6.0874$, $LL_s^{\text{Optimal}}=-18.4026$, $LL_s^{\text{Parallel}}=-28.4325$, $LL_s^{\text{ETAS}}=-55.4833$ and $jLL_s^{\text{Total}}=-1.8580$, $LL_s^{\text{Parallel}}=-9.1080$, $LL_s^{\text{Optimal}}=-9.1643$, $LL_s^{\text{ETAS}}=-35.6646$, for time periods 0-10 and 10-20 days, respectively. The spatial distribution of log-likelihoods within our study grid is presented in Fig. 7 for the aforementioned time intervals and, (4) The relative performance of the forecasts exhibits large spatial variability within physics-based models, but they also yield information gain over the benchmark ETAS model between $G=0.75-1.25$ (Fig. S2, available in the electronic supplement to this article).

Further evaluation of our updated prospective forecast including all available catalog data for the first 6 months following the mainshock shows that the benchmark statistical model ETAS together with the standard physics-based approaches present low rejection ratios ($R_{\text{ETAS}}=R_{\text{Parallel}}=R_{\text{Optimal}}\sim 1\%$) for the daily N test (Fig. S3). However, they are rejected due to underestimation of observed seismicity at the 2 most critical time intervals immediately following the mainshock and the largest triggered event of the sequence. On the other hand the total stress method has comparable performance ($R_{\text{Total}}=8\%$) with the upside of passing the N test the first day after the mainshock.

Lastly, our 30-year time dependent probability calculation on the stress-increased areas of the main boundary thrust west of the 25 April 2015 $M=7.8$ mainshock, show that values have been increased from the pre-Gorkha level 5-8%, up to as much as 29%. In Fig. 4 we present the aforementioned time dependent probability considering the average, maximum co-seismic stress changes and alternative recurrence parameters.

Conclusions

Formal testing of the prospective forecast using 60 days of triggered earthquake occurrence shows strong performance of physics-based methods in anticipating the highest magnitude events ($M>6$). All methods struggled with capturing the cumulative number of triggered earthquakes, either underestimating or overestimating during the first 20 days. Spatial performance evaluations are difficult in low productivity sequences because slowly stressed regions can take years to produce enough earthquakes for the predictability of these models to be fully assessed.

Statistical methods rely heavily on precursory activity to identify future larger earthquake locations; the $M=7.3$ Kodari shock was not preceded by detectable seismicity, meaning that event was only forecasted by physics-based methods. The calibration of statistical forecasts using the near-real time available earthquake catalog was a great challenge but also gave us the opportunity to prospectively test the efficiency of empirical cascading models under poor detection thresholds. We do not regard our findings as evidence of ETAS failure; instead they are more an illustration under which conditions statistical models can reach their best performance.

However, standard physics-based approaches and the total stress method also forecast higher probability in areas that have so far not experienced large aftershocks, and therefore score low against some formal testing metrics. More time and more earthquakes will enable a more complete evaluation. Although no single event should be used to validate a prospective forecast, we are of course most interested in the expected occurrence of the largest magnitude triggered events. In that context, the $M=7.3$ Kodari and $M=5.6$ Xegar earthquake exemplified the contribution of stress-based approaches in identifying possible nucleation sites even in the absence of precursor seismicity.

These tradeoffs lead us to conclude that forecasts should rely on hybrid models that combine physical and statistical models in time and space.

Data and resources

In this study we have used the finite source models for the mainshock and the largest aftershock as well as seismic parameters for this earthquake sequence available at the USGS web-site [<http://earthquake.usgs.gov>, last accessed August 2015].

Acknowledgements

We thank Eric Geist and Ruth Harris for their helpful comments, two anonymous reviewers, the Associate Editor Sue Hough and the Editor of SRL Zhigang Peng for their suggestions regarding the presentation of the manuscript.

References

- Ader, T., Avouac, J.P., Liu-Zeng J., Lyon-Caen H., Bollinger, L. et al., (2012). Convergence rate across the Nepal Himalaya and interseismic coupling on the Main Himalayan Thrust: implications for seismic hazard, *J. Geophys. Res.* 117, B04403
- Bollinger L., Sapkota, S.N., Tapponier, P., Klinger, Y. Rizza, M. *et al.* (2014) Estimating the return times of great Himalayan earthquakes in eastern Nepal: evidence from the Patu and Bardibas strand of the Main Frontal Thrust, *J. Geophys. Res.* 119, 7123–7163.
- Bilham, R., Gaur, V. K., Molnar, P. (2001). Himalayan seismic hazard, *Science* 293, 1442-1444.
- Bakun, W. H. & Wentworth, C. M. (1997) Estimating earthquake location and magnitude from seismic intensity data, *Bull. Seismol. Soc. Am.* 87, 1502-1521.
- Bollinger, L., J. P. Avouac, R. Cattin, M. R. Pandey (2004). Stress buildup in the Himalaya, *J. Geophys. Res.* 109, B11405, doi:10.1029/2003JB002911.
- Dieterich J. H. (1994). A constitutive law for rate of earthquake production and its application to earthquake clustering, *J. Geophys. Res.* 99, 2601–2618.
- Dieterich J. H. & Kilgore B. (1996) Implications of fault constitutive properties for earthquake prediction, *Proc. Nat. Acad. of Sci. USA* 93, 3787-3794.
- Cocco M., Hainzl S., Catalli, F. Enescu, B. Lombardi, A.M. et al. (2010) Sensitivity study of forecasted aftershock seismicity based on Coulomb stress calculation and rate- and state-dependent frictional response, *J. Geophys. Res.* 115, B05307, 10.1029/2009JB006838.
- Console, R., Murru M. and G. Falcone (2010). Perturbation of earthquake probability for interacting faults by static Coulomb stress changes, *J. Seis.*, 14(1). 67-77.
- Hardebeck, J. L. (2004). Stress triggering and earthquake probability estimates, *J. Geophys. Res.*, 109, B04310, doi:10.1029/2003JB002437.
- Hardebeck, J. L. (2014) The impact of static stress change, dynamic stress change, and the background stress on aftershock focal mechanisms, *J. Geophys. Res.* 119, 8239–8266, doi:10.1002/2014JB011533.
- Harris R. A. (1998). Introduction to special section: stress triggers, stress shadows, and implications for seismic hazard, *J. Geophys. Res.* 103, 24,347-24-358.
- Harris R. A. & Simpson R. W. (1996). In the shadow of 1857 - the effect of the great Ft. Tejon earthquake on subsequent earthquakes in Southern California, *Geophys. Res. Lett.* 23, 229-232.
- Helmstetter A. (2003) Is earthquake triggering driven by small earthquakes?, *Phys. Rev. Lett.* 91, 585011-585014.
- Jaeger, J. C. & Cook, N. G. W. (1976). *Fundamentals of Rock Mechanics*, Chapman and Hall, London, England.
- Jordan, T. H., Y.T. Chen, P. Gasparini, R. Madariaga, I. Main, W. Marzocchi, G. Papadopoulos, G. Sobolev, K. Yamaoka and J. Zschau (2011). Operational Earthquake Forecasting. State of Knowledge and Guidelines for Utilization. *Annals of Geophysics*, 54(4), doi:10.4401/ag-5350.
- Jouanne, F., Mugnier, J.L., Gamond, J.F., Le Fort, P., Pandey, M.R. *et al.*, (2004). Current shortening across the Himalayas of Nepal, *Geophys. J. Int.* 157, 1–14
- Kagan, Y. Y. (2003). Accuracy of modern global earthquake catalogs, *Phys. Earth Planet. Int.* 135, 173-209 (2003).
- King, G. C. P. and Stein, R. S. and Lin, J. (1994). Static stress changes and the triggering of earthquakes, *Bull. Seismol. Soc. Am.* 84, 935-953.

- Mallman E. P. and Zoback M. D. (2007). Assessing elastic Coulomb stress transfer models using seismicity rates in southern California and southwestern Japan, *J. Geophys. Res.* 112, B03304, doi:10.1029/2005JB004076.
- Mallman, E. P. and Parsons, T. (2008). A global search for stress shadows, *J. Geophys. Res.* 113, doi:10.1029/2007JB005336.
- Martin S. and Szeliga, W. (2010). A catalog of felt intensity data for 570 earthquakes in India from 1636 to 2009, *Bull. Seismol. Soc. Am.* 100, 562-569.
- Nanjo K. Z., Tsuruoka, H. Yokoi, S., Ogata, Y., Falcone, G. *et al.* (2012). Predictability study on the aftershock sequence following the 2011 Tohoku-Oki, Japan, earthquake: first results, *Geophys. J. Int.* 191, 653-658.
- National Society for Earthquake Technology-Nepal (NSET) (2010). Shelter response strategy and plan for earthquake disasters for Kathmandu Valley, Nepal, 60 pp.
- Ogata Y. (1988) Statistical models for earthquake occurrences and residual analysis for point processes, *J. Amer. Statist. Assoc.* 83, 9-27.
- Ogata Y. (1998) Space-time point-process models for earthquake occurrences, *Ann. Inst. Stat. Math.* 50, 379-402.
- Omori F. (1894) On aftershocks, Report of Imperial Earthquake Investigation Committee 2, 103-109.
- Parsons, T., Toda, S., Stein, R. S., Barka, A., and Dieterich, J. H. (2000). Heightened odds of large earthquakes near Istanbul: an interaction-based probability calculation, *Science* 288, 661-665.
- Parsons, T. (2005). Significance of stress transfer in time-dependent earthquake probability calculations, *J. Geophys. Res.* 110, B05S02, doi:10.1029/2004JB003190.
- Parsons, T., Ji C. & Kirby E. (2008). Stress changes from the 2008 Wenchuan earthquake and increased hazard in the Sichuan basin, *Nature* 454, 509-510.
- Parsons, T., Ogata, Y., Zhuang, J. & Geist, E. L. (2012) Evaluation of static stress change forecasting with prospective and blind tests, *Geophys. J. Int.* 188, 1425-1440, doi: 10.1111/j.1365-246X.2011.05343.x.
- Parsons, T. & Segou M. (2014). Stress, distance, magnitude, and clustering influences on the success or failure of an aftershock forecast: the 2013 $M=6.6$ Lushan Earthquake and other examples, *Seis. Res. Lett.* 85, 44-51.
- Rajendran, C. P., John B. and Rajendran K. (2015). Medieval pulse of great earthquakes in the central Himalaya: viewing past activities on the frontal thrust, *J. Geophys. Res.* 120.
- Rhoades, D.A., D. Schorlemmer, M.C. Gerstenberger, A. Christophersen, J.D. Zechar, and M. Imoto (2011). Efficient testing of earthquake forecasting models, *Acta Geophysica* 59, 728-747, doi:10.2478/s11600-011-0013-5.
- Sapkota S. N., Bollinger, L., Klinger, Y., Tapponier, P. and Gaudemer, Y. *et al.* (2013). Primary surface ruptures of the great Himalayan earthquakes in 1934 and 1255, *Nature Geosci.* 6, 71-76.
- Schorlemmer, D., Gerstenberger, M.C., Wiemer, S., Jackson, D.D., Rhoades, D.A. (2007). Earthquake likelihood model testing, *Seismol. Res. Lett.* 78, 17-29.
- Segou, M. Parsons, T. and Ellsworth, W. (2014). Comparative evaluation of physics-based and statistical forecasts in Northern California, *J. Geophys. Res.* 118, 6219-6240, doi:10.1002/2013JB010313

- Sornette D. & Werner M. J. (2005) Constraints on the size of the smallest triggering earthquake from the epidemic-type aftershock sequence model, Båth's law, and observed aftershock sequences, *J. Geophys. Res.* 110, B08304, doi 10.1029/2004JB003535.
- Strader, A., and D. D. Jackson (2015), Static Coulomb stress-based Southern California earthquake forecasts: A pseudoprospective test, *J. Geophys. Res. Solid Earth*, 120, 1667–1676, doi:10.1002/2014JB011297.
- Stein, R. S. (1999). The role of stress transfer in earthquake occurrence, *Nature* 402, 605-609.
- Stramondo S., Christodoulos, K. Bignami, C., Chini, M. Melini D. et al. (2011) Did the September 2010 (Darfield) earthquake trigger the February 2011 (Christchurch) event?, *Scientific Reports* 1, Article number 98.
- Toda, S., Stein, R. S., Richards-Dinger, K. & Bozkurt, S. (2005). Forecasting the evolution of seismicity in southern California: animations built on earthquake stress transfer, *J. Geophys. Res.* 110, B05S16, doi:10.1029/2004JB003415.
- Toda S. & Enescu, B. (2011). Rate/state Coulomb stress transfer model for the CSEP Japan seismicity forecast, *Earth Planets Space* 63, 171-185.
- Utsu T. (1961). Statistical study on the occurrence of aftershocks, *Geophys. Mag.* 30, 521–605.
- Wobus, C., Heimsath, A., Whipple, K. & Hodges, K. (2005). Active out-of-sequence thrust faulting in the central Nepalese Himalaya, *Nature* 434, 1008-1011.
- Woessner, J., S. Hainzl, W. Marzocchi, M. J. Werner, A.M. Lombardi *et al.* (2011), A Retrospective Comparative Forecast Test on the 1992 Landers Sequence, *J. Geophys. Res.*, B05305, doi:10.1029/2010JB007846.
- Yeats R. S., T. Nakata, A. Farah, M. Fort, M.A. Mirza *et al.*, The Himalayan frontal fault system, *Annales Tectonicae* VI, 85-98 (1992).
- Zechar, J. D., Gerstenberger, M. C., Rhoades, D. A. (2010). Likelihood-based tests for evaluating space-rate-magnitude earthquake forecasts, *Bull. Seismol. Soc. Am.* 100, 1184-1195.

FIGURES

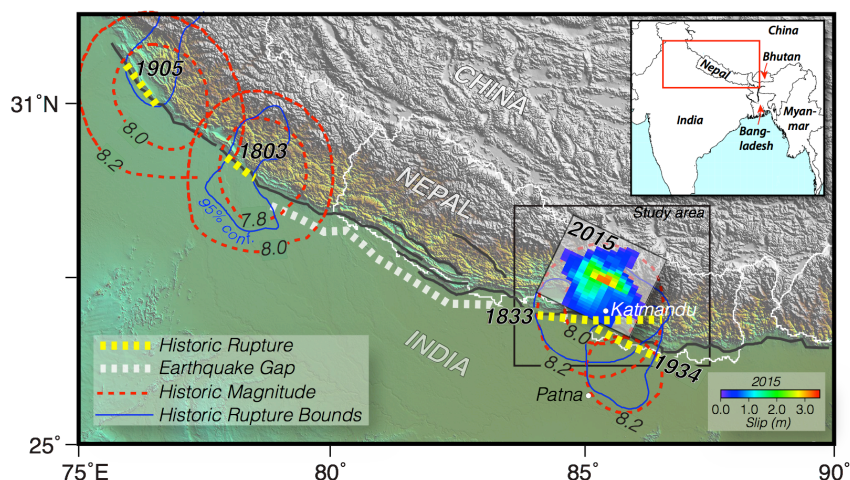


Fig. 1. Setting of the 25 April 2015 $M=7.8$ earthquake in Nepal. The rupture plane (dipping 10° down to the northeast) and slip distribution, provided by USGS³, are shown in relation to historic ruptures (yellow dashed lines give possible rupture ranges, and not necessarily rupture lengths). Blue lines show 95% confidence bounds on rupture locations and red contours give magnitude vs. epicenter location. Large ($M\sim 8$) earthquakes have clustered near the east end of a broad seismic gap (white dashed line) at the central Himalayan front that has not ruptured since AD1255-1505 (see *Historic earthquake location* section, available in the electronic supplement to this article).

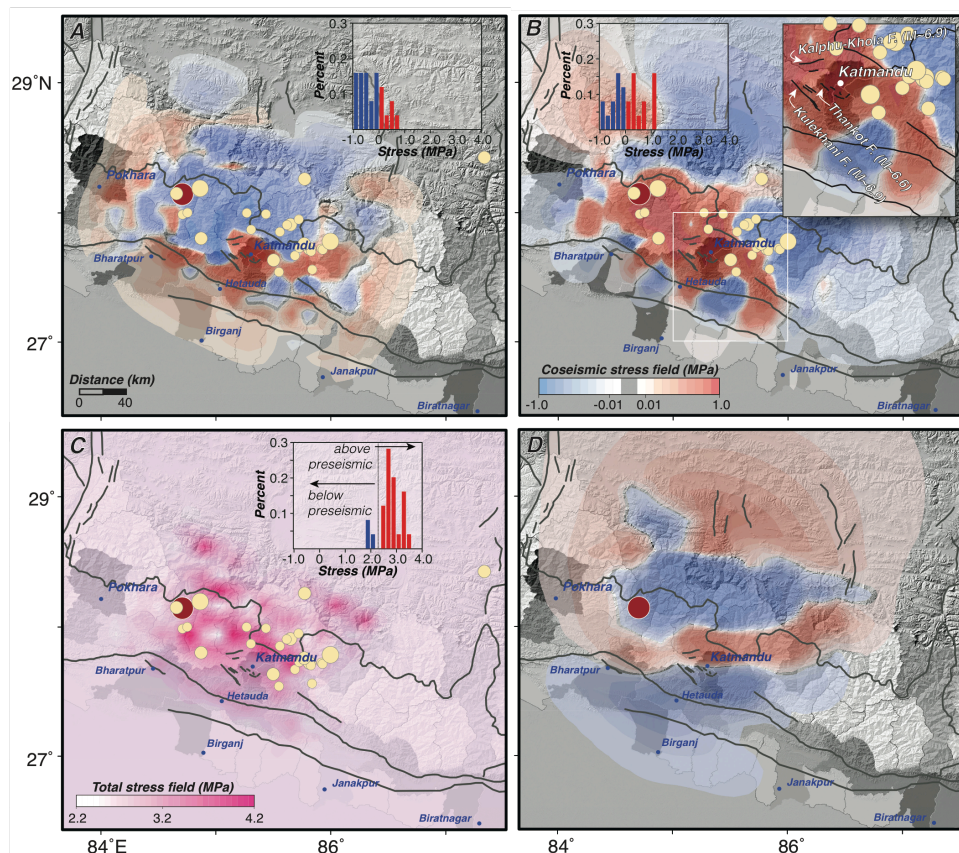


Fig. 2. Calculated Coulomb stress change distribution from different methods. Triggered earthquakes above the magnitude completeness level of $M\geq 4.7$ are shown as dots, and the mainshock as a red dot. Relative population density by prefecture in Nepal is shown, with densest areas shaded more darkly. Histograms show the number of triggered events in stress-increased and stress-

³ http://earthquake.usgs.gov/earthquakes/eventpage/us20002926#scientific_finitefault

http://earthquake.usgs.gov/earthquakes/eventpage/us20002ejl#scientific_finitefault

decreased areas. Major faults are shown as black lines. **(a)** Stress changes are resolved on planes parallel to the mainshock rupture at 10 km depth. **(b)** Stress changes are resolved on faults optimally orientated to a horizontal greatest stress direction of N19°E at 10 km depth. A close-up of the Katmandu basin and local faults with maximum magnitude assignments is shown. **(c)** Total stress (pre-seismic and coseismic change) resolved at 10 km depth on planes most favorable to resultant principal stress directions and magnitudes. **(d)** Stress changes resolved on the decollement fault that extends north beneath the Himalayas.

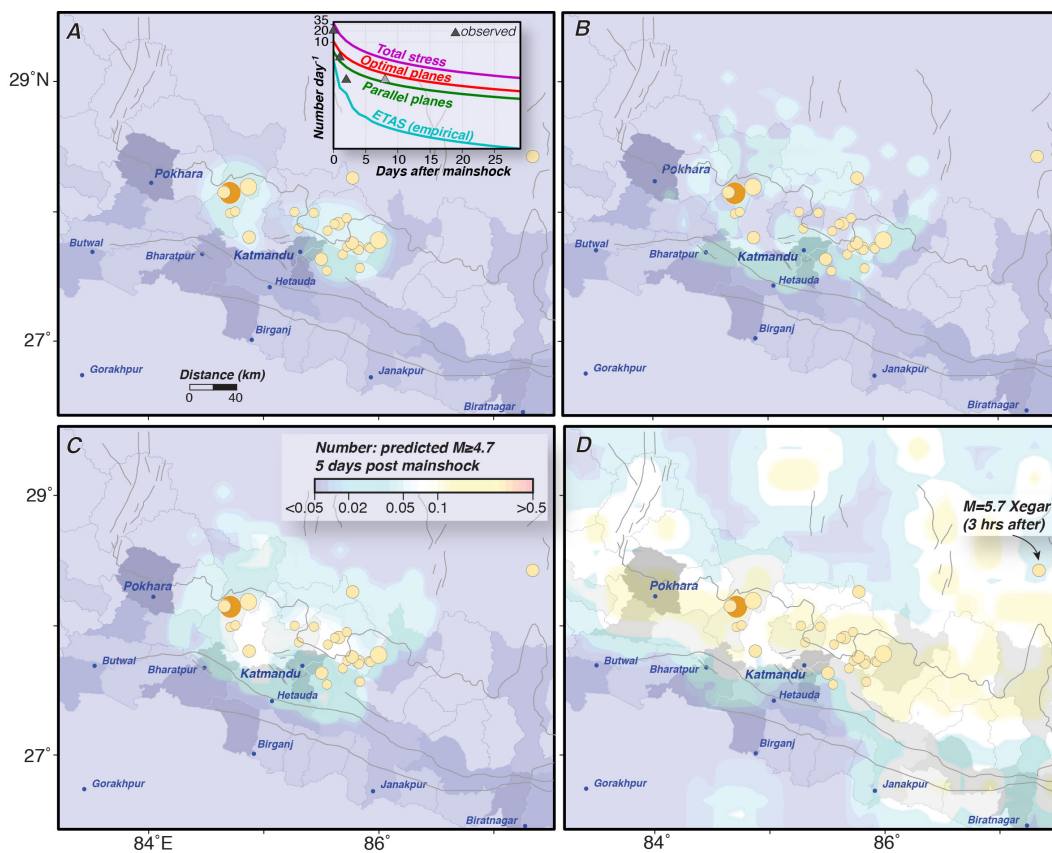


Fig. 3. Five-day forecast comparisons. Contours show expected numbers of $M \geq 4.7$ events, and the actual distribution of triggered earthquakes is plotted. **(a)** The statistical forecast is spatially limited because it depends on precursory earthquakes. The inset shows the 30-day forecast; dark triangles represent events used to tune the statistical forecast, and the lighter triangle shows a subsequent rate. **(b)** A forecast based on stress changes resolved on planes parallel to the mainshock is improved relative to the statistical method, but still underreports the first days of seismicity. Forecasts based on **(c)** optimal fault orientations and **(d)** the complete stress tensor bracket observed $M \geq 4.7$ rates, with the total stress

method forecasting a much wider area that captures the $M=5.7$ Xegar shock, located ~ 245 km east of the mainshock.

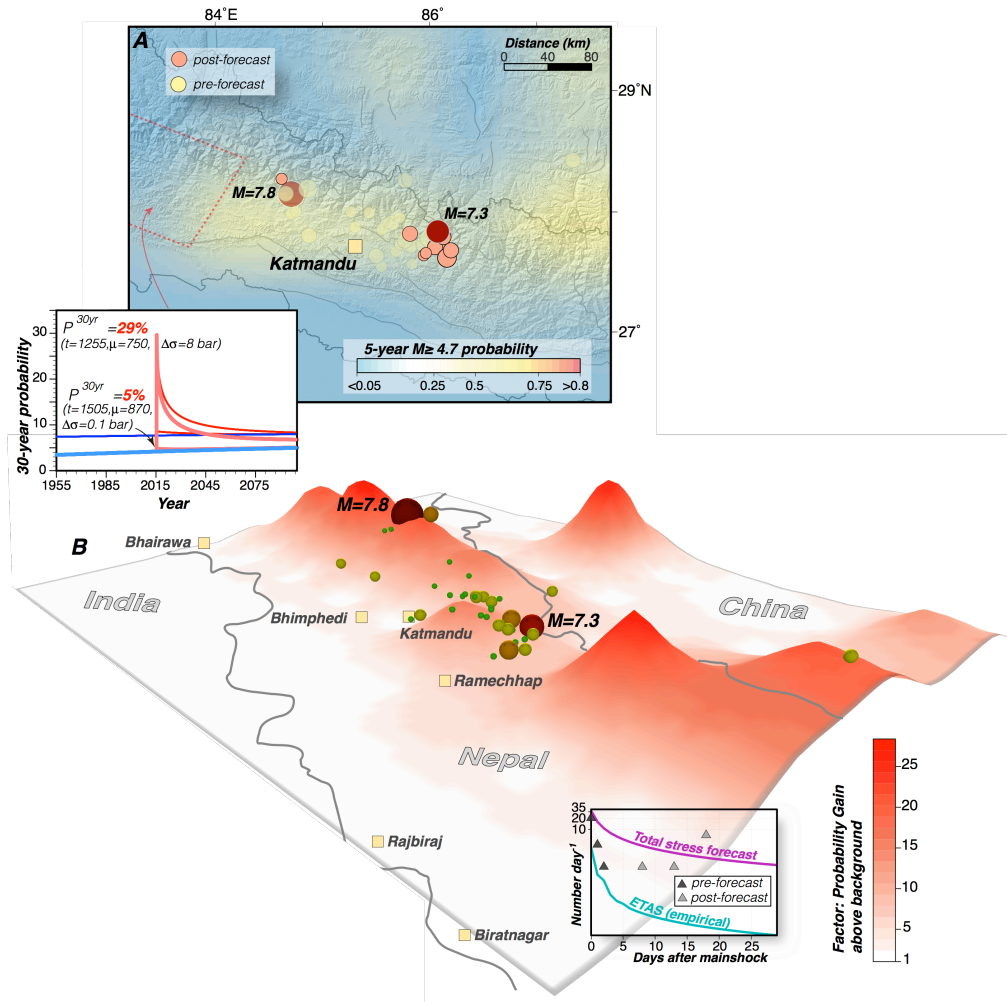


Fig. 4. Five year probabilistic forecast for the Katmandu region and affected areas along the Himalayan front. (a) 5-yr $M \geq 4.7$ Probability calculated before 9 May 2015 is contoured. A band of heightened probability tracks along the Himalayan front that is of particular concern at the seismic gap west of the 25 April 2015 $M=7.8$ mainshock. The lower inset shows time dependent probability (Method) vs. year specific to stress-increased parts of the main boundary thrust range reach a maximum of 29% (increased from 5-8%) in the next 30 years. **(b)** Ratio of 5-year $M \geq 4.7$ earthquake probability to background level is shown as a contour surface to illustrate most likely future earthquakes sites. The 12 May $M=7.3$ shock and all other $M \geq 4.7$ events (spheres) fell within areas of ≥ 5 -fold gain. Comparative 30-day forecast rate decay vs. time curves (calculated using

first 5 days of observed seismicity) are shown with updated observations that include the 12 May $M=7.3$ shock.

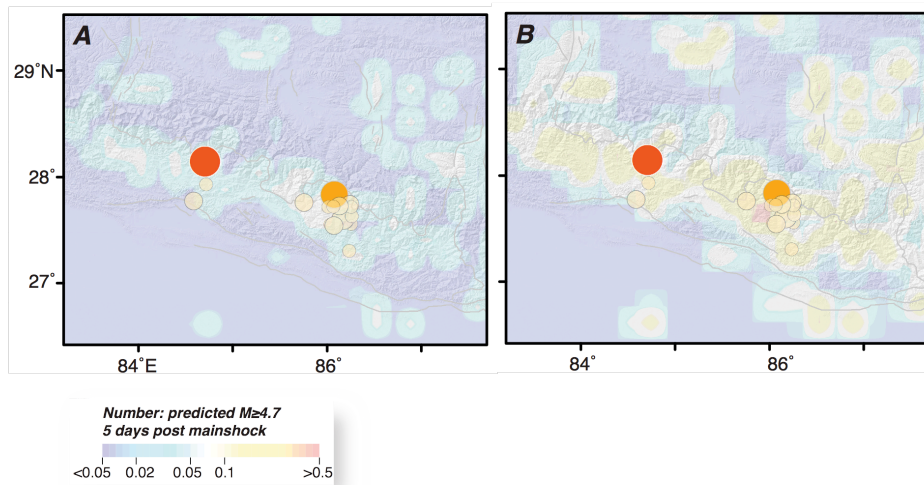


Fig. 5. Five day forecast comparison. Contours show expected numbers of $M \geq 4.7$ events, and the actual distribution of triggered earthquakes is plotted for the first 5 days following the $M=7.3$ triggered event (12/05/2015 07:05:19 UTC). The initial and updated forecast, based on the total stress method, incorporate (a) co-seismic stress changes only by the $M=7.8$ mainshock and (b) additional stress changes by the $M=7.3$ triggered event.

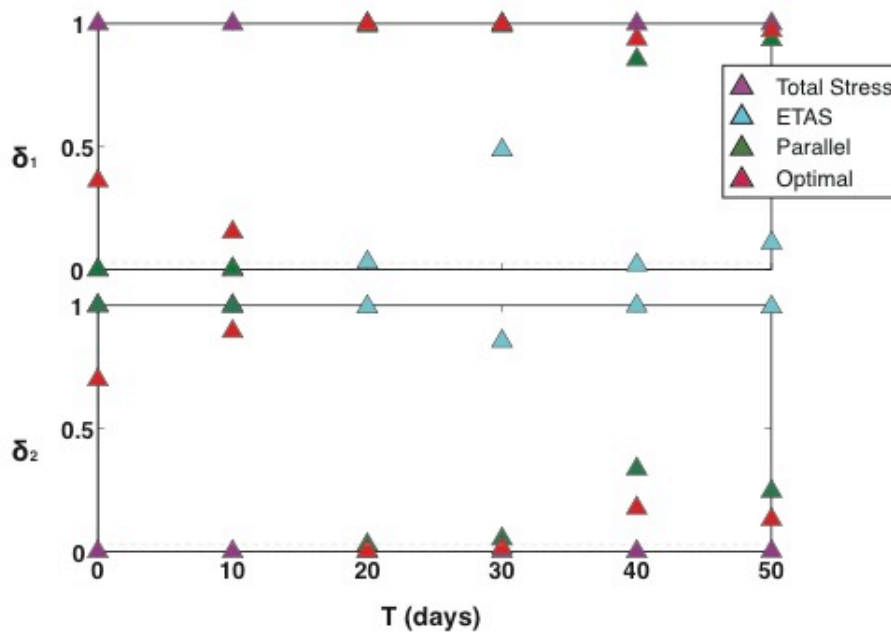


Fig. 6. Absolute performance evaluation of forecast models. Quantile scores of δ_1 and δ_2 of the N -test as a function of time evaluated within 10-day intervals. Gray dashed line indicates the 0.05 significance level at which a forecast is rejected. Small δ_1 and δ_2 values correspond to underestimation and overestimation of the observed seismicity by a forecast model, respectively. The benchmark ETAS model underestimates observed seismicity through the entire testing period, and the model from stress changes resolved on parallel faults also suffers for the same reason at the early stages of the sequence, whereas the total-stress and the optimal planes method show signs of overestimation.

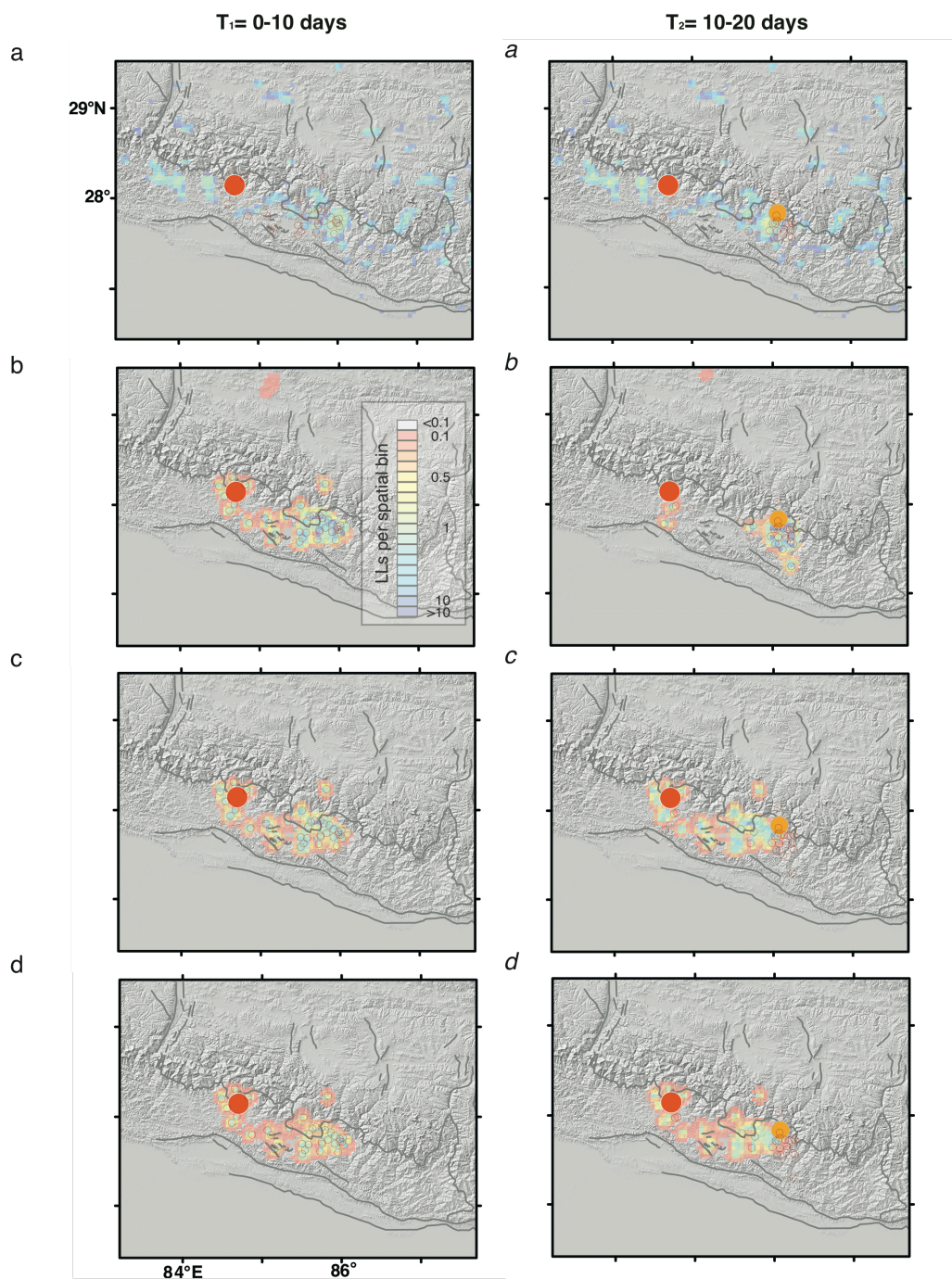


Fig. 7. Relative Performance evaluation of forecast models. Triggered earthquakes above the magnitude of completeness of $M \geq 4.7$ are shown as dots. Major faults are shown as black lines. Maps of log likelihood at each spatial bin

1 **Electronic Supplement to**

2

3 **Prospective earthquake forecasts at the Himalayan front after**
4 **the 25 April 2015 $M=7.8$ Gorkha mainshock**

5

6 **By M. Segou and T. Parsons**

7

8 The electronic supplement (Part A) focuses on **Historic earthquake location**, the
9 implementation of **Epidemic Type Aftershock Sequence**, the **Conversion of Stress Changes**
10 **in Forecast Earthquake Rates**, an example of San Francisco Bay area related to the **Total**
11 **Stress** method implementation [Figure S1], a short-term forecast evaluation of the predictability
12 of the forecast models using **Performance evaluation metrics**, such as information gain [Figure
13 S2] together with a long-term (6 months) evaluation [Figure S3]. At the second part of this
14 electronic supplement (Part B) we present the **original forecast as of 9 May, 2015 (56 hours**
15 **before the 12 May 2015 $M=7.3$ aftershock).**

16

17

PART A

18

19 **Historic earthquake location.** We calculate historic earthquake locations from historical
20 intensity observations (Bakun and Wentworth, 1997; Martin and Szeling, 2010). The
21 method performs a grid search for trial epicenters (5 km spacing in east and north
22 directions) and, using an empirical intensity attenuation relation vs. distance, locates the
23 region where 95% of trial epicenters minimize root mean square (RMS) misfits to observed
24 intensity values.

25

26 **Epidemic Type Aftershock Sequence (ETAS) implementation.** Short-term statistical
27 earthquake forecasts built on the idea that each earthquake triggers a number of off-spring
28 events, relative to its magnitude, and on empirical laws such as the Omori law decay and
29 the Gutenberg-Richter magnitude frequency distribution. Here, we allow the ETAS (Ogata,
30 1988; Ogata, 1998) model to use all available earthquakes to achieve optimum
31 performance although the Nepal catalog is complete to $M \geq 4.7$. To estimate the necessary

32 parameters, we use equations for estimating the apparent fraction n_a with respect to the
 33 real fraction of triggered events n (Sornette and Werner, 2005).

34 Analytically following the Epidemic Type Aftershock Sequence (ETAS) model the space-
 35 time seismicity rate $\lambda(x,y,t)$ is given by:

$$37 \quad \lambda(x, y, t) = \mu(x, y) + \sum_{i:t_i < t} \frac{Ke^{\alpha(M_i - M_{th})}}{(t - t_i + c)^p} f_i(x - x_i, y - y_i; M_i),$$

$$38 \quad \text{with } f(x, y; M) = \frac{q-1}{\pi D(M)} \left(1 + \frac{x^2 + y^2}{D(M)}\right)^{-q}$$

39 and $D(M) = de^{\gamma(M - M_{min})}$. In our implementation parameter values are as follows: $M_{max} = 7.8$,
 40 $M_{min} = 4.7$, $m_d = 4.0$, $\alpha = 0.7$, $b = 1.0$, $n = 0.67$, $n_a = 0.51$, $k = 0.2167$, $c = 0.002$ day. Parameter $\mu(x,y)$ is the
 41 background rate, c , and p are Omori-law values governing the decay rate of aftershocks, α
 42 estimates the magnitude efficiency of an earthquake in generating its offspring; d , γ and q
 43 ($d = 0.0071$ deg², $q = 1.96$, $\gamma = 0.7$) are spatial fitting parameters in close agreement with parameters
 44 from similar seismotectonic environments (Parsons and Segou, 2014).

45 For the favorable case of lower magnitude scaling formulation with $\alpha < b = 1.0$, the apparent
 46 branching ratio n_a is given by the equation

$$47 \quad n_a = \frac{kb \ln(10)(M_{max} - m_d)}{1 - 10^{-b(M_{max} - M_{min})}} \quad \text{and the relation between } n \text{ and } n_a \text{ is}$$

$$48 \quad n_a = n \left(\frac{10^{(b-a)(M_{max} - m_d)} - 1}{10^{(b-a)(M_{max} - M_{min})} - 1} \right), \text{ where } m_d \text{ is the detection threshold and } M_{min} \text{ the minimum}$$

49 triggering threshold.

50

51

52 **Conversion of stress changes to forecast earthquake rates.** Following the rate-and-
 53 state friction framework (Dieterich, 1994; Dieterich, 1996) the pre-mainshock earthquake
 54 activity R , as $R = \frac{r}{\gamma \dot{\tau}}$ where

55 $\gamma_n = \gamma_{n-1} \exp\left(\frac{-\Delta CFF}{A\sigma}\right)$, is suppressed or enhanced by static stress changes.

56

57 The time-dependent seismicity rate $R(t)$ is a function of state variable γ after a stress perturbation

58 $\gamma_{n+1} = \left[\gamma_n - \frac{1}{\dot{\tau}}\right] \exp\left[\frac{-\Delta t \dot{\tau}}{A\sigma}\right] + \frac{1}{\dot{\tau}}$ where r is the steady-state seismicity rate, ΔCFF is the stress

59 step, aftershock duration t_a is assumed to be 25 years, and daily forecast parameters are: $a\sigma=0.5$

60 (Toda and Enescu, 2011) and $\dot{\tau}=0.00239$ MPa/yr, based on regional thrust fault slip rates of ~ 10

61 mm/yr (Ader *et al.*, 2012). $R(t)$ is related to earthquake probability over the interval Δt as

62 $P(t, \Delta t) = 1 - \exp\left[-\int_t^{t+\Delta t} R(t) dt\right] = 1 - \exp(-N(t))$,

63 where $N(t)$ is expressed as

$$N(t) = r_p \left\{ \Delta t + t_a \ln \left[\frac{1 + \left[\exp\left(\frac{-\Delta CFF}{A\sigma}\right) - 1 \right] \exp\left[\frac{-\Delta t}{t_a}\right]}{\exp\left(\frac{-\Delta CFF}{A\sigma}\right)} \right] \right\}$$

64

65 and $r_p = \left(\frac{-1}{\Delta t}\right) \ln(1 - P_c)$, where P_c is a conditional probability.

66

67 **Performance evaluation metrics**

68 The modified N -test (Zechar *et al.*, 2010) evaluates the consistency between the total number

69 of predicted and observed events within the area of interest. This test is based on the equations,

70 $\delta_1 = 1 - F(N_{Obs} - 1 | N_F)$ and $\delta_2 = F(N_{Obs} | N_F)$, where $F(x|\mu)$ is the right-continuous Poisson

71 cumulative distribution function with expectation μ evaluated at x and N_F is the forecast
72 number of events determined by the model. The quantiles δ_1 and δ_2 answer two questions under
73 the assumption that the forecast is correct: (1) What is the probability of observing at least N_{obs}
74 events? And (2) what is the probability of observing at most N_{obs} earthquakes? These metrics
75 share a complimentary role $\delta_1 \simeq 1 - \delta_2$ suggesting a forecast be rejected if either $\delta_1(t) < \alpha_{eff}$
76 or $\delta_2(t) < \alpha_{eff}$, where $\alpha_{eff}=0.025$ corresponds to the effective significance value. In Fig. S2 we
77 show the results of the N -test within 10-day time windows.

78

79 The S -test (Zechar *et al.*, 2010) aims to compare the relative spatial performance of the
80 forecast model using log-likelihood statistics estimated over 1000 simulations. The log-
81 likelihood L of observing ω events at a given expectation λ for a model j is defined by the
82 logarithm of the probability $p(\omega|\lambda)$ expressed by

83

$$L(\omega|\lambda^j) = \log p(\omega|\lambda^j) = -\lambda^j + \omega \log \lambda^j - \log \omega!$$

84 and,

$$L(\Omega|\Lambda) = \sum_{(i,j \in R)} \left(-\lambda(i,j) + \omega(i,j) \log(\lambda(i,j)) - \log(\omega(i,j)!) \right)$$

85

86 in the case of the joint log-likelihood, which represents the sum of log-likelihood values over all
87 bins b_i . We present in Fig. S3 maps of the log-likelihood per spatial bin for the time intervals 0-
88 10 and 10-20 days, respectively.

89

90 The T -test (Rhoades *et al.*, 2011) evaluates the sample information gain per earthquake of a
 91 model A over model B defined by
 92 $I_N(A, B) = \frac{1}{N} \sum_{i=1}^N (X_i - Y_i) - \frac{\hat{N}_A - \hat{N}_B}{N}$ (6), where $I_N(A, B)$ is considered as the mean of a
 93 sample from a population with actual mean $I(A, B)$, where $I_N(A, B)$ is the true information gain
 94 of model A over model B with with $X_i = \log \lambda_A(i)$ and $Y_i = \log \lambda_B(i)$ the log-likelihood value of
 95 a model A and B in the i^{th} bin. Here, we use the statistical model as reference model due to the
 96 simplicity of this implementation. We present in Fig. S4, the mean and the 95% confidence
 97 interval of the information gain per model for the time intervals used in our spatial mapping of
 98 log-likelihood.

99
 100
 101
 102

Fig. S1. Effects of stress change on different rake, dip on San Francisco Bay region stress changes following the 1906 earthquake. The dominant optimal plane strikes northwest, has a right-lateral rake, and dips vertically. Coulomb stress changes calculated on these planes are negative. However, because the San Andreas fault ruptured through a restraining bend, the same fault orientations with 45° dips and pure thrust rakes have positive Coulomb failure stress.

103
 104
 105
 106
 107
 108
 109
 110
 111

Fig. S2. Information Gain. Mean and 95% confidence interval of the information gain of physics-based forecasts when the statistical model is taken as reference for (a) 0-10 days and (b) 10-20 days time period. Note the low standard deviation for the Total Stress model (<0.004).

112
 113
 114
 115
 116
 117

Fig. S3. Long-term Performance Evaluation. Prospective forecast update (a) for the statistical benchmark model (cyan), parallel (green), optimal (red) and total stress (magenta) method overlaid with observation (triangles) above $M=4.7$. In (b) and (c) the quantiles δ_1 and δ_2 the N test as a function of time, respectively. Gray dashed line indicates the 0.05 significance level at which a forecast is rejected.

118
 119
 120
 121
 122
 123

124

125

PART B

126

127

128 **Prospective forecast as of 9 May, 2015 (56 hours before the 12 May 2015 $M=7.3$**
129 **aftershock).**

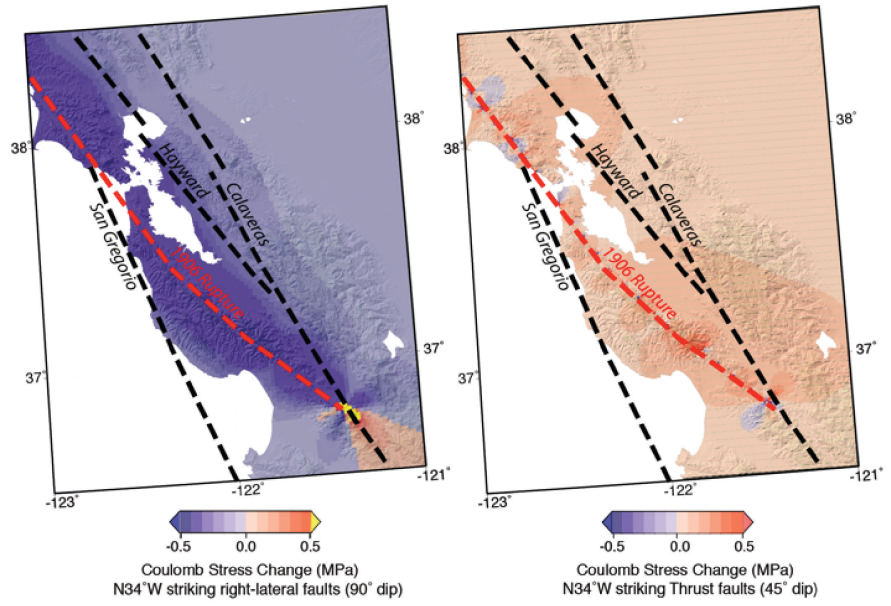
130

131 This is the original rapid forecast that was completed 2 weeks after the 25 April $M=7.8$ Nepal
132 mainshock. It is followed by an email confirming the submission time before the 12 May $M=7.3$
133 aftershock.

134

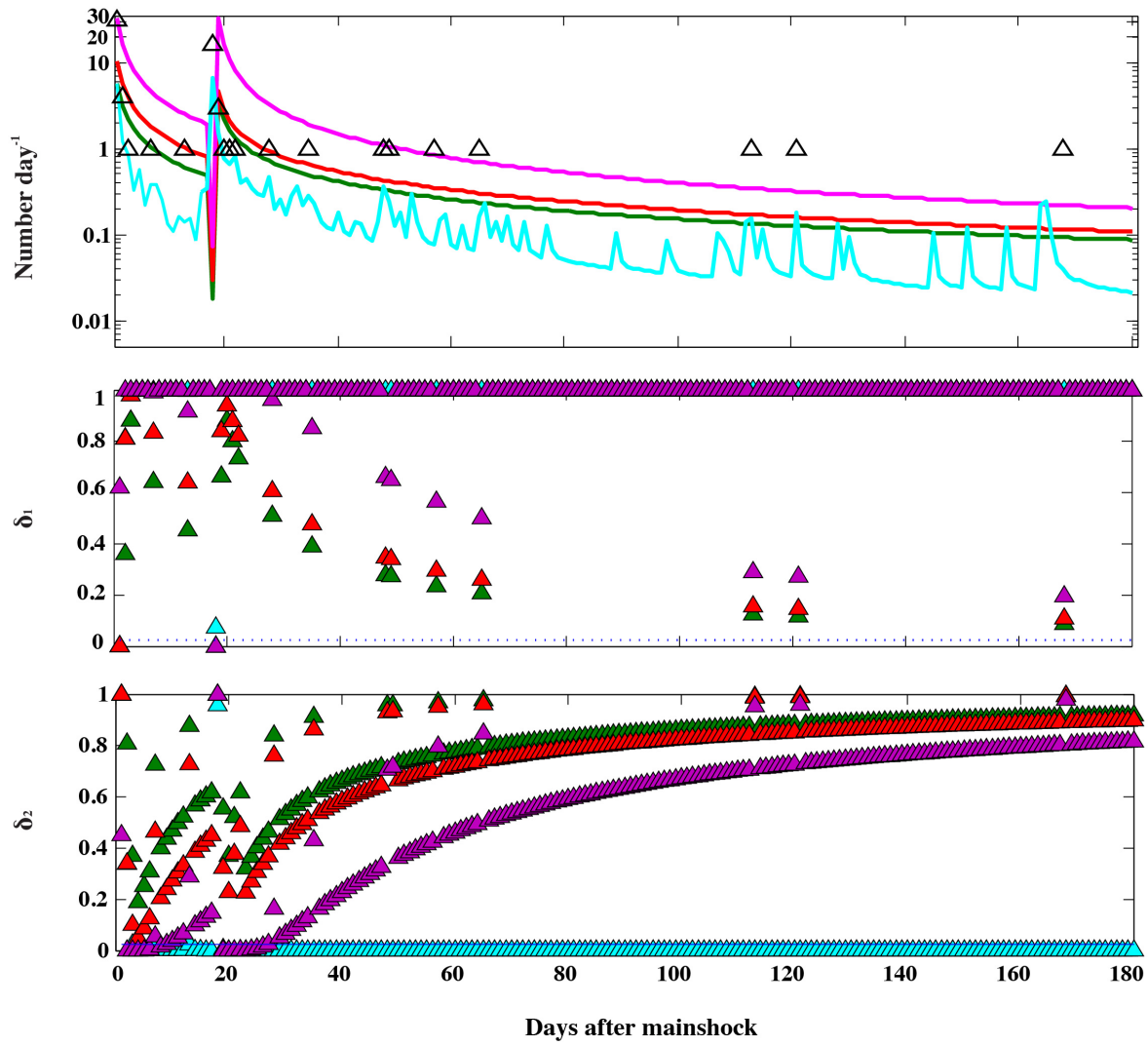
135

within 0-10 (left panel) and 10-20 days (right panel) are shown for the **(a,a)** complete stress tensor forecast, **(b,b)** statistical model, **(c,c)** physics forecast based on planes parallel to the mainshock rupture, **(d,d)** physics forecast based on optimal fault orientations. The sum of log-likelihood at the end of the evaluation phase (0-20 days) at the location of Kodari $M=7.3$ (12/05/2015 07:05:19 UTC) triggered event, noted as an orange circle in the right panel, is associated with smaller log-likelihood values for the complete stress tensor forecast model, indicating good performance (LL_s^A : -2.0616, LL_s^B : -11.336, LL_s^C : -2.7621, LL_s^D : -2.7592).



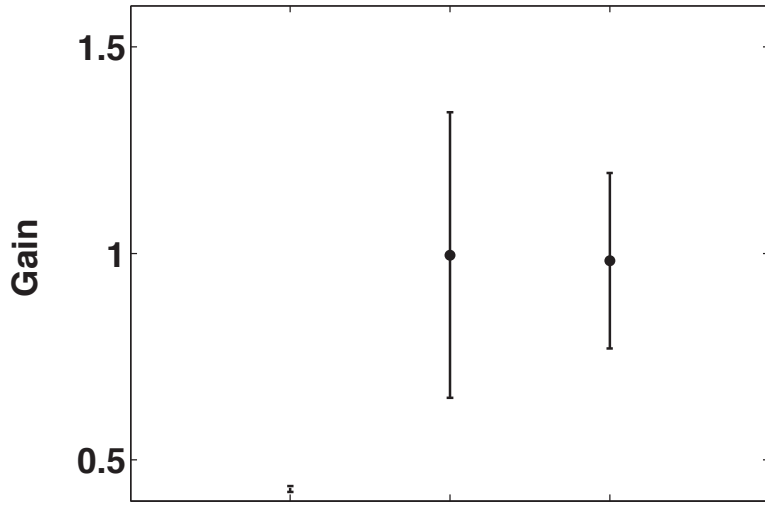
Coulomb Stress Change (MPa)
 N34°W striking right-lateral faults (90° dip)

Coulomb Stress Change (MPa)
 N34°W striking Thrust faults (45° dip)

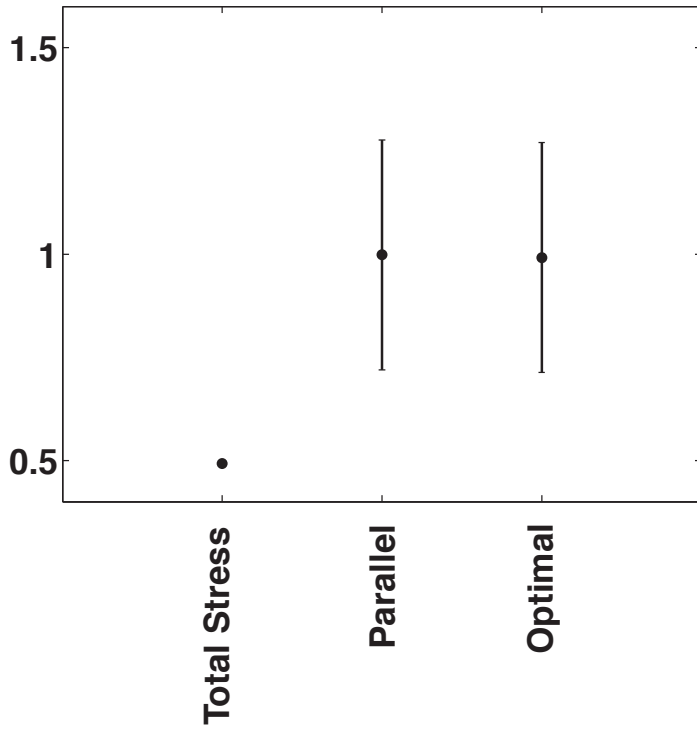


a

Rererence Model: ETAS



b



1 *Impending earthquakes beneath Katmandu and the Himalayan front after the 25*
2 *April 2015 $M=7.8$ Nepal mainshock*

3
4 M. Segou and T. Parsons

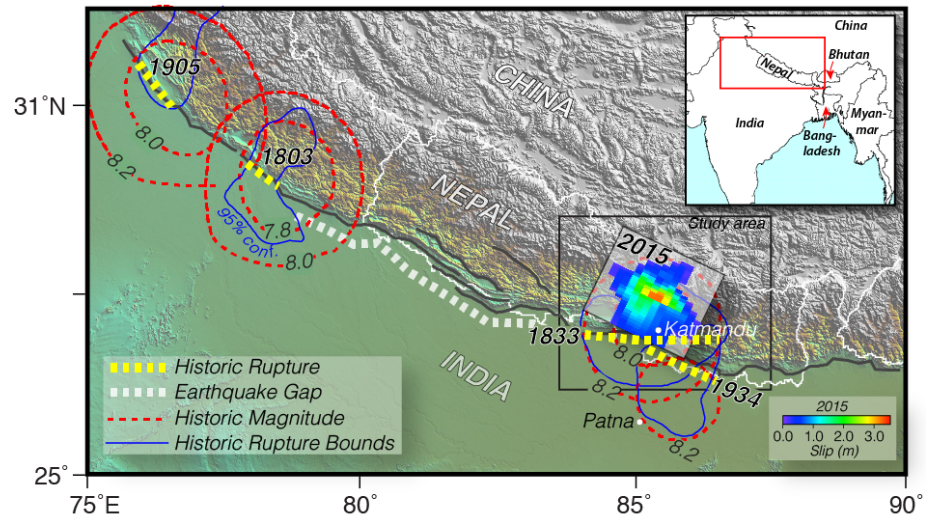
5 U.S. Geological Survey, Menlo Park, California

6
7 When a major earthquake strikes, the resulting devastation is compounded or
8 even exceeded by the subsequent cascade of triggered seismicity. As the
9 Nepalese begin recovery from the 25 April 2015 shock, knowledge of what
10 comes next is essential. We calculate the redistribution of crustal stresses and
11 earthquake probabilities for different time horizons from daily to 30 years into the
12 future. The odds of moderate to large earthquakes affecting Katmandu reach
13 90%, and exceed 50% for the Himalayan front in eastern Nepal. The probability
14 of a great earthquake filling part of the seismic gap west of Katmandu may have
15 been increased to 14% in the next 30 years.

16 A slow motion crash between the Indian and Eurasian plates is absorbed at a
17 18-22 mm/yr rate (1) by great earthquakes that raise the Himalayas (FigSB. 1).
18 On the 25th of April, 2015, a $M=7.8$ earthquake ruptured the low-angle (10°) fault
19 contact between the two plates, leading to 7,696 confirmed fatalities, 16,727
20 people injured, and more than a million families affected (2). Eight UNESCO
21 World Heritage sites were damaged or destroyed. The 2015 shock struck on the
22 eastern edge of a wide gap between historic earthquakes (3) along the Himalayan
23 front (FigSB. 1). Potentially compounding this catastrophe is the possibility of
24 subsequent, lethal triggered earthquakes beneath highly populated basins in the
25 central Himalaya akin to recent tragedies in Turkey (4), China (5), and New
26 Zealand (6). Large triggered earthquake rates are highest immediately after
27 mainshocks, decay exponentially with time, and can persist for years (7). Here we
28 calculate the expected redistribution of stress in the Himalayan crust and develop

29 a novel method to anticipate where and when triggered earthquakes are most
30 likely to happen that is especially applicable to frontier regions.

31



32

33 **FigSB. 1. Setting of the 25 April 2015 $M=7.8$ earthquake in Nepal.** The
34 rupture plane (dipping 10° down to the northeast) and slip distribution (δ) at the
35 Himalayan front are shown in relation to historic (3) ruptures (yellow dashed lines
36 give the possible rupture range, and not necessarily the rupture length). Blue lines
37 show 95% confidence bounds on rupture locations and red contours give
38 magnitude vs. epicenter location. Large ($M\sim 8$) Earthquakes have clustered near
39 the east end of a broad seismic gap (white dashed line) at the central Himalayan
40 front that has not ruptured since $\sim AD1255-1505^9$.

41

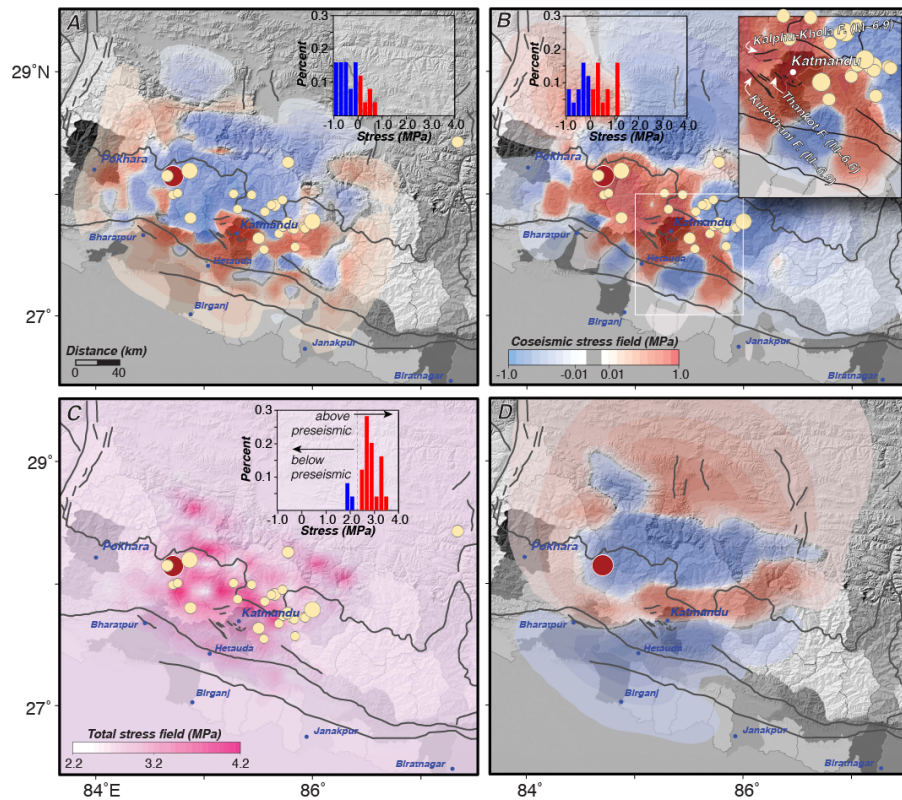
42 Short term earthquake forecasts, known as Operational Earthquake Forecasts
43 (10), use empirical statistics to anticipate cascades of triggered events (11).
44 Physical simulations of stress redistribution (12) following a mainshock combined
45 with conceptual frictional models also describe triggered earthquake occurrence
46 (13). Both methods encounter difficulty accurately accounting for the full
47 spectrum of post mainshock earthquake behavior (5). Statistics depend on the
48 density of the local earthquake recording network and identification of precursory

49 activity, and thus are vulnerable in frontier regions. Physical models depend on
50 our ability to accurately simulate a mainshock rupture and its transfer of stress
51 onto crustal faults. Usually these forecasts rely on Coulomb failure stress changes
52 calculated on hypothetical, optimally oriented faults that align with an estimated
53 regional stress (12) wherein faults may be brought closer to, or further from
54 failure. Constitutive fault parameters are also required (13).

55 A persistent problem with physical models is that triggered earthquakes
56 happen in areas of calculated stress reduction (known as stress shadows), where
57 theoretically they should be suppressed. We thus develop a new approach that
58 considers the total (preseismic and coseismic) stress field, rather than just the
59 coseismic changes. Solutions for most favorable fault rake and dip are found from
60 the principal axes of the full stress tensor (14). In this mode there are no expected
61 regions of earthquake suppression because there is always a possible fault
62 orientation that is favorable for failure. Certain classes of earthquake mechanism
63 may be suppressed, but others are encouraged (15).

64 For example, traditional stress change calculations resolved on faults parallel
65 to the mainshock and onto optimal faults cannot fully explain the first 5 days of
66 triggered earthquakes. In both cases significant numbers (72% and 48%
67 respectively) of events occur where stress reductions are calculated (FigSB 2a-b).
68 The total stress field calculations yield a better match; only 12% of triggered
69 events occurred where the total stress is less than preseismic levels (FigSB. 2c).
70 All stress change methods show the Katmandu prefecture under a coseismic stress
71 increase (FigSB. 2). At the southwest edge of the Katmandu basin, the Thankot

72 fault ($M_{max}\sim 6.6$) (16) is calculated to have increased by an average 0.15 MPa.
 73 Further to the southwest, calculations show that the Kulekhani fault ($M_{max}\sim 6.9$)
 74 (16) stress was increased by 0.32 MPa. Stress on the Kalphu-Khola fault
 75 ($M_{max}\sim 6.9$) (16) north of Katmandu was increased by 0.28 MPa. Nepal's second
 76 largest city, Pokhara, lies to the west of the 25 April rupture, and is characterized
 77 by coseismic stress increases, but smaller than in the Katmandu basin. We
 78 calculate up to 0.1 MPa coseismic stress



79

80
 81
 82
 83
 84
 85
 86
 87

FigSB. 2. Calculated Coulomb stress change distribution from different methods. Triggered earthquakes above the magnitude completeness level of $M\geq 4.7$ are shown as dots, and the mainshock as a red dot. Relative population density by prefecture in Nepal is shown, with densest areas shaded more darkly. Histograms show the number of triggered events in stress-increased and stress-decreased areas. Major faults are shown as black lines. **(A)** Stress changes are resolved on planes parallel to the mainshock rupture at 10 km depth. **(B)** Stress changes are resolved on faults optimally orientated to a horizontal greatest stress

88 direction of N19°W (21) at 10 km depth. A close-up of the Katmandu basin and
89 local faults with maximum magnitude assignments (16) is shown. (C) Total stress
90 (pre-seismic and coseismic change) resolved at 10 km depth on planes most
91 favorable to resultant principal stress directions and magnitudes. (D) Stress
92 changes resolved on the decollement fault that extends north beneath the
93 Himalayas.

94

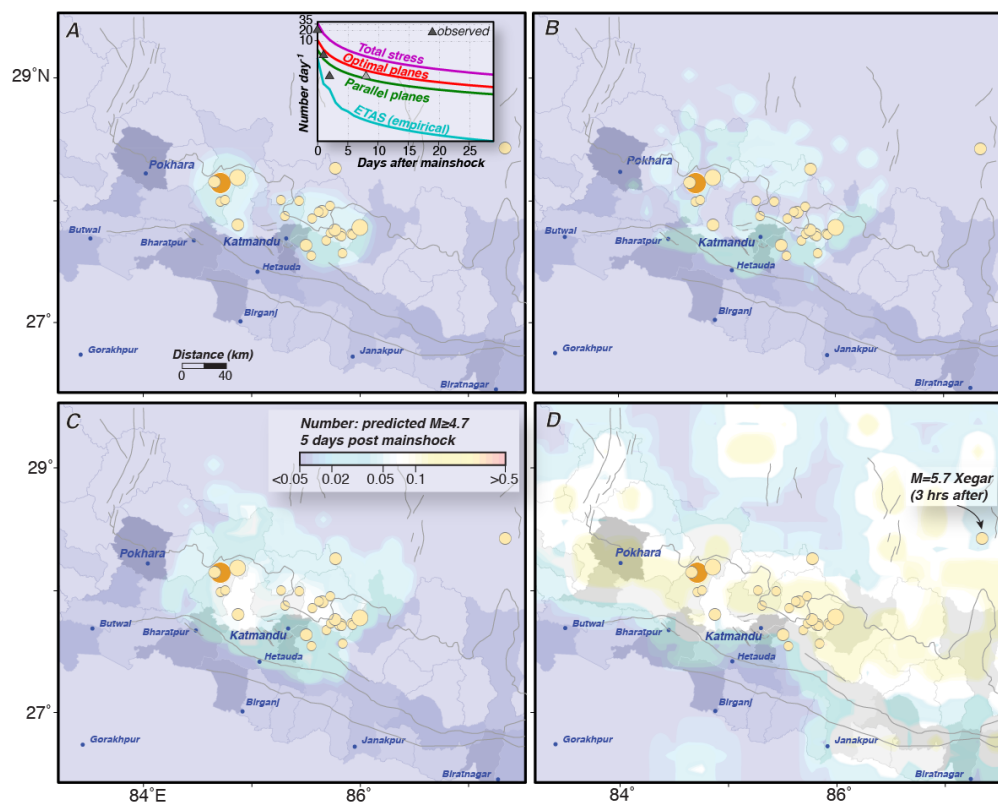
95 increase on the deep decollement beneath the Himalayas (FigSB 2d), and a 6.5
96 bar increase on the main boundary thrust immediately west of the 2015
97 mainshock rupture. As destructive as the 2015 earthquake was, interpretation of
98 paleoseismological (9) and historical shaking intensity (3) observations shows
99 that earthquakes well above $M=8$ occur routinely along the Himalayan front (17)
100 (FigSB. 1).

101 An operational earthquake forecast involves different time horizons depending
102 on the application, from emergency response (days), restoration (<1 year),
103 reconstruction (~1-3 years) and mitigation (~3+ years). Here we present forecasts
104 from pure empirical/statistical (11), standard physical (13), and new total stress
105 field methods (14) to compare effects of method on result. Durations cover short
106 (5 days), intermediate (1 month), and long term (5 years).

107 Statistical models (11) perform especially well with comprehensive
108 earthquake networks capable of recording all shocks to $M=2$ levels. However in
109 frontier regions where these smaller magnitude events go unreported (18), these
110 models significantly underforecast (FigSB. 3a). The two 5-day forecasts we
111 produce based on standard physics (FigSB. 3b-c) also underforecast the early
112 triggered earthquake rates and are spatially limited, failing to capture the breadth
113 of the complete triggered earthquake region. The total-stress forecast predicts

114 higher $M \geq 4.7$ earthquake rates along an extended part the Himalayan front, and
 115 predicts triggered seismicity in the rift basins that cut across the Himalayas
 116 (FigSB. 3d). After the first few hours post-mainshock there is evidence for
 117 widespread triggered seismicity, evidenced by the $M=5.7$ Xegar event 245 km
 118 east of the mainshock.

119



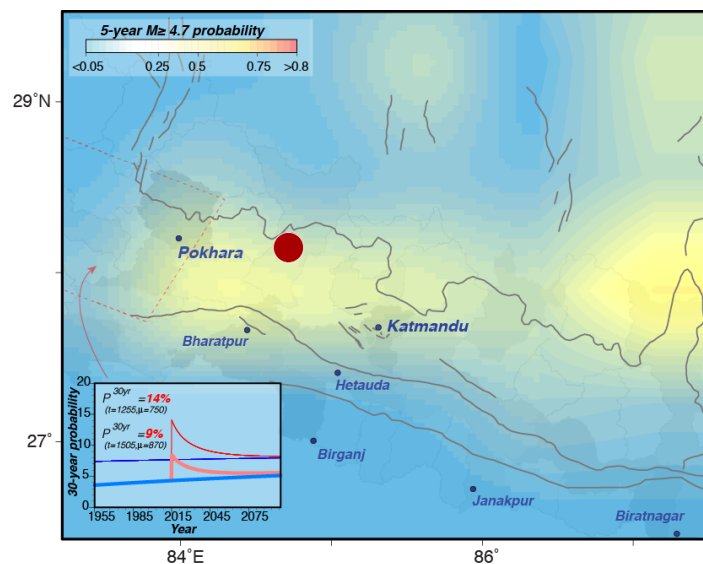
120

121 **FigSB. 3. Five-day forecast comparisons.** Contours show expected numbers
 122 of $M \geq 4.7$ events, and the actual distribution of triggered earthquakes is plotted.
 123 Relative population density is shown with highest areas darker. (A) The statistical
 124 forecast is spatially limited because it depends on the empirical distribution of
 125 triggered earthquakes. The inset shows the 30-day forecast rate; dark triangles
 126 represent events used to tune the statistical forecast, and the lighter triangle
 127 shows a subsequent rate. (B) A forecast based on stress changes resolved on
 128 planes parallel to the mainshock rupture is improved relative to the statistical
 129 method, but still underreports the first days of seismicity. Forecasts based on (C)
 130 optimal fault orientations and (D) the complete stress tensor bracket observed
 131 $M \geq 4.7$ rates, with the total stress method forecasting a much wider geographic

132 area that captures the $M=5.7$ Xegar shock, located ~245 km east of the
133 mainshock.

134

135 We calculate $M \geq 4.7$ earthquake probability for the coming 5 years using our
136 preferred total stress method, and 30-year time dependent probability (19) on the
137 stress-increased areas of the main boundary thrust west of the 25 April 2015
138 $M=7.8$ mainshock that has not ruptured since at least AD1505 (FigSB. 4) (9).
139 Results include up to a 14% chance (increased from 8%) of a great earthquake
140 west of Katmandu, and the prospective 5-year earthquake probability map shows
141 a swath parallel to the Himalayan front that is expected ($\geq 50\%$ chance) to
142 experience moderate to strong earthquakes. Aggregated probability from mapped
143 faults (16) in the Katmandu Basin shows a 90% chance of at least one more
144 $M \geq 4.7$ shock in the next 5 years. Validation of the 5-year forecast through
145 tracking future seismicity will assess the predictive skills of our forecast.



146

147 **FigSB. 4. Five year probabilistic forecast for the Katmandu region and**
 148 **affected areas along the Himalayan front.** Probability of $M \geq 4.7$ earthquakes
 149 during the next 5 years is contoured. Generally, a band of heightened probability
 150 tracks along the Himalayan front that is of particular concern west of the 25 April
 151 2015 $M=7.8$ mainshock, given that a great earthquake has not occurred there in
 152 hundreds of years. The lower inset shows time dependent probability (19) vs.
 153 time specific to stress-increased parts of the main boundary thrust range from 9-
 154 14% (increased from 4-8%) in the next 30 years (recurrence parameters adopted
 155 from (9)).

156

157 **REFERENCES AND NOTES**

- 158 1. Ader, T., et al. (2012), Convergence rate across the Nepal Himalaya and interseismic
 159 coupling on the Main Himalayan Thrust: Implications for seismic hazard, *J. Geophys.*
 160 *Res.*, 117, B04403, doi:10.1029/2011JB009071.
- 161 2. Figures from Nepal Red Cross Society.
- 162 3. We use the method of W. H. Bakun and C. M. Wentworth, *Bull. Seis. Soc. Am.* 87, 1502
 163 (1997) to calculate historic earthquake locations from historical intensity observations
 164 compiled by S. Martin and W. Szeliga, *Bull. Seis. Soc. Am.* 100, 562 (2010).
- 165 4. Parsons, T., S. Toda, R. S. Stein, A. Barka, and J. H. Dieterich, *Science* 288, 661, (2000).
- 166 5. Parsons, T., C. Ji, and E. Kirby, *Nature* 454, 509 (2008), Parsons, T., and M. Segou, *Seis.*
 167 *Res. Lett.* 85, 44 (2014).
- 168 6. Stramondo, S., C. Kyriakopoulos, C. Bignami, M. Chini, D. Melini, M. Moro, M. Picchiani,
 169 M. Saroli, and E. Boschi, *Scientific Reports* 1, Article number 98. (2011).
- 170 7. Omori, F., On aftershocks, Report of Imperial Earthquake Investigation Committee, 2,
 171 103-109, 1894. Utsu, T., 1961, Statistical study on the occurrence of aftershocks,
 172 *Geophys. Mag.*, 30, 521–605. Parsons, T. (2002), Global Omori law decay of triggered
 173 earthquakes: Large aftershocks outside the classical aftershock zone, *Journal of*
 174 *Geophysical Research*, 107, 2199, doi:10.1029/2001JB000646.
- 175 8. http://earthquake.usgs.gov/earthquakes/eventpage/us20002926#scientific_finitefault
- 176 9. Rajendran, C. P., B. John, and K. Rajendran (2015), Medieval pulse of great earthquakes
 177 in the central Himalaya: Viewing past activities on the frontal thrust, *J. Geophys. Res.*,
 178 120. Bollinger, L., S. N. Sapkota, P. Tapponnier, Y. Klinger, M. Rizza, J. Van der Woerd,
 179 D. R. Tiwari, R. Pandey, A. Bitri, and S. Bes de Berc (2014), Estimating the return times
 180 of great Himalayan earthquakes in eastern Nepal: Evidence from the Patu and Bardibas
 181 strand of the Main Frontal Thrust, *J. Geophys. Res. Solid Earth*, 119, 7123–7163. Primary
 182 surface ruptures of the great Himalayan earthquakes in 1934 and 1255, S. N. Sapkota, L.
 183 Bollinger, Y. Klinger, P. Tapponnier, Y. Gaudemer and D. Tiwari (2013), *Nature*
 184 *Geoscience*, 6, 71-76.
- 185 10. T. H. Jordan, W. Marzocchi, A. J. Michael, and M. C. Gerstenberger (2014), Operational
 186 earthquake forecasting can enhance earthquake preparedness, *Seis. Res. Lett.*, 85, 955-
 187 959.
- 188 11. We use the Epidemic Type Aftershock (ETAS) model (20), where the space-time
 189 seismicity rate $\lambda(x,y,t)$ is given by $\lambda(x,y,t) = \mu(x,y) + \sum_{i:t_i < t} \frac{\kappa e^{\alpha(M_i - M_0)}}{(t - t_i + c)^p} f_i(x - x_i, y - y_i; M_i)$,

190
191
192
193
194
195
196
197
198
199
200
201
202
203
204
205
206
207
208

209
210
211
212
213
214
215
216
217
218
219
220
221
222
223
224
225
226

227
228
229

where $f(x,y;M) = \frac{q-1}{\pi D(M)} \left(1 + \frac{x^2 + y^2}{D(M)}\right)^{-q}$, and $D(M) = de^{\gamma(M-M_{min})}$. Parameter μ is the

background rate, κ , c , and p are Omori-law values ($\bar{\tau}$) governing the decay rate of aftershocks, a estimates the magnitude efficiency of an earthquake in generating its offspring; d , γ and q are spatial fitting parameters. The Nepal catalog is complete to $M \geq 4.7$, but we allowed the ETAS model to use all available earthquakes to achieve optimum performance.

12. Stein, R. S., 1999, The role of stress transfer in earthquake Occurrence, Nature, 402, 605-609.

13. Coulomb failure stress ($\Delta CF \equiv \Delta|\bar{\tau}_f| + \mu'(\Delta\sigma_n)$, $\mu' = \mu(1 - B_k)$) where $\Delta\bar{\tau}_f$ is the change in shear stress on the receiver fault, μ is the coefficient of friction, $\Delta\sigma_n$ is the change in normal stress, and B_k is Skempton's coefficient (accounts for pore fluid pressure). Stress values are found by slipping an elastic dislocation representation of the mainshock slip model (8). Friction coefficient is taken to be 0.4. A 10 MPa deviatoric tectonic stress with compression oriented N19°W (21) is used to find optimally oriented receiver fault planes. The same magnitude and direction is used for the total stress method. Additionally, we calculate stress change on planes parallel to, and on the mainshock fault to find likely future rupture areas on the main boundary fault and other possibly hidden faults of like orientation (22). Following the rate-and-state friction framework (23) the pre-mainshock earthquake activity R , as $R = \frac{r}{\gamma\bar{\tau}}$, where

$\gamma_n = \gamma_{n-1} \exp\left(\frac{-\Delta CF}{a\sigma}\right)$, is suppressed or enhanced by static stress changes. The decay

rate of this effect is inversely correlated with the shear stressing rate ($\dot{\tau}$). Daily forecast parameters are: $a\sigma = 0.5$ (24) and $\dot{\tau} = 0.00239$ MPa/yr, based on regional thrust fault slip rates of ~ 10 mm/yr (1).

14. The total stress tensor is the sum of the presesimic stress and stress change tensors $\sigma_{x,y,z}^T = \sigma_{x,y,z}^{PRE} + \Delta\sigma_{x,y,z}$. The strike angle between principal stress axes and the favored fault plane β is from $\tan 2\beta = 1/\mu$ (25). A grid search is performed in 5° steps over dip and rake to maximize Coulomb failure for all possible mechanism classes (reverse, normal, and transform) (26).

15. Mallman, E. P., and T. Parsons (2008), A Global Search for Stress Shadows, J. Geophys. Res., v. 113, doi:10.1029/2007JB005336.

16. National Society for Earthquake Technology-Nepal (NSET), Shelter response strategy and plan for earthquake disasters for Kathmandu Valley, Nepal, 60 pp. (2010).

17. R. Bilham, Vi. K. Gaur, P. Molnar, Himalayan seismic hazard, Science, 293, 1442-1444.

18. Kagan, Y. Y. (2003), Accuracy of modern global earthquake catalogs, Phys. Earth Planet. Int., 135, 173-209.

19. Time-dependent seismicity rate $R(t)$ after a stress perturbation is

$$R(t) = \frac{r}{\left[\exp\left(\frac{-\Delta CFF}{a\sigma}\right) - 1\right] \exp\left[\frac{-t}{t_a}\right] + 1} \quad (23) \text{ where } r \text{ is the steady-state seismicity rate,}$$

ΔCFF is the stress step, aftershock duration t_a is assumed to be 25 years, and $a\sigma = 0.5$ (24). $R(t)$ is related to earthquake probability over the interval Δt as

$$P(t, \Delta t) = 1 - \exp\left[-\int_t^{t+\Delta t} R(t) dt\right] = 1 - \exp(-N(t)) \quad (27) \text{ where}$$

230
231
232
233
234
235
236
237
238
239
240
241
242
243
244
245
246
247
248
249
250
251
252
253
254
255

$$N(t) = r_p \left\{ \Delta t + t_a \ln \left[\frac{1 + \left[\exp\left(\frac{-\Delta CFF}{a\sigma}\right) - 1 \right] \exp\left[\frac{-t}{t_a}\right]}{\exp\left(\frac{-\Delta CFF}{a\sigma}\right)} \right] \right\}, \text{ and } r_p = \left(\frac{-1}{\Delta t}\right) \ln(1 - P_c) \text{ where } P_c \text{ is a}$$

conditional probability. We calculate time dependent probability using a Brownian Passage Time distribution with aperiodicity=0.5 and bracket the calculations with mean recurrence intervals ranging from 750-870 years and last earthquake times either 1255 or 1505 (9).

20. Ogata Y., 1988, Statistical models for earthquake occurrences and residual analysis for point processes, *J. Amer. Statist. Assoc.*, 83, 9-27. Ogata, Y., (1998). Space-time point-process models for earthquake occurrences, *Ann. Inst. Stat. Math.*, 50, 379-402.
21. F. Jouanne, J. L. Mugnier, J. F. Gamond, P. Le Fort, M. R. Pandey, L. Bollinger, M. Flouzat and J. P. Avouac, Current shortening across the Himalayas of Nepal, *Geophys. J. Int.* (2004) 157, 1-14.
22. C. Wobus, A. Heimsath, K. Whipple, and K. Hodges, Active out-of-sequence thrust faulting in the central Nepalese Himalaya, *Nature*, 434, 1008-1011.
23. Dieterich, J. (1994), A constitutive law for rate of earthquake production and its application to earthquake clustering, *J. Geophys. Res.*, 99, 2601-2618.
24. S. Toda, B. Enescu, Rate/state Coulomb stress transfer model for the CSEP Japan seismicity forecast, *Earth Planets Space*, Vol. 63 (No. 3), pp. 171-185, 2011.
25. Jaeger, J. C., and N. G. W. Cook, *Fundamentals of Rock Mechanics*, Chapman and Hall, London, England, 1976.
26. Aki, K., and P. G. Richards, 1980, *Quantitative Seismology*, 932 pp., W.H. Freeman & Co., New York.
27. Dieterich, J. H., and B. Kilgore (1996), Implications of fault constitutive properties for earthquake prediction, *Proc. Nat. Acad. of Sci. USA*, 93, 3787-3794.

From: science_editors@aaas.org
Subject: Successful Submission of a Manuscript to Science
Date: May 9, 2015 at 4:18 PM
To: tparsons@usgs.gov

Manuscript Title: Impending earthquakes beneath Katmandu and the Himalayan front after the 25 April 2015 M=7.8 Nepal mainshock
Author: Parsons
Manuscript Number: aac5455

Dear Dr. Parsons:

Thank you for your submission to Science. We have successfully received your Report.

You can see the status of your manuscript at any time by logging into your account at the Science Journals Submission and Information Portal at <https://cts.sciencemag.org>. Your manuscript number is noted above. Your manuscript is now undergoing an initial screening to determine whether it will be sent for in-depth review. If the manuscript is sent to review, its status will change to "To Review".

We encourage you to login and link your account to your ORCID ID, an identifier that facilitates correct attribution of your publications. To learn more about ORCID or to obtain an ORCID ID, visit their site at: <http://orcid.org>.

Sincerely,
The Editors
Science